Radiation Physics and Chemistry 239 (2026) 113332

Contents lists available at ScienceDirect

Radiation Physics and Chemistry

journal homepage: www.elsevier.com/locate/radphyschem

Framework for optimal design of a multi-source rectangular X-ray cargo scanning system

Caroline Bossuyt *, Arnold J. den Dekker, Domenico Iuso, Jan De Beenhouwer, Jan Sijbers

imec-Vision Lab, Department of Physics, University of Antwerp, Antwerp, 2610, Belgium
DynXLab: Center for 4D Quantitative X-ray Imaging and Analysis, Antwerp, 2610, Belgium

ARTICLE INFO

Keywords:
Optimal experiment design
Multi-source
Rectangular
X-ray CT
Cargo scanning

ABSTRACT

The first line of non-destructive inspection of cargo often relies on single or double-view X-ray radiography, which is fast but lacks depth resolution and is prone to object occlusion. In contrast, conventional X-ray computed tomography (CT) allows 3D imaging but typically relies on mechanically rotating gantries, which limits throughput and increases system complexity. Recently, multi-source fixed-gantry X-ray systems have been proposed as a promising acquisition geometry to combine high imaging speed with volumetric imaging, while reducing mechanical complexity. The precision of the reconstructed images stemming from these systems as a function of the acquisition setup has however hardly been explored. This paper proposes a flexible framework for optimal experiment design of a rectangular multi-source X-ray cargo scanning system. The proposed framework allows the experimenter to calculate the highest attainable imaging precision, as quantified by the Cramér–Rao lower bound (CRLB), as a function of the X-ray system's geometric settings, which facilitates optimal experiment design. To illustrate this potential, several system configurations with differently positioned and oriented sources are evaluated and compared in terms of the CRLB-based A-optimality criterion.

1. Introduction

As the number of transported containers worldwide increases, so does the number of organized criminal activities at ports, stressing the need for container inspection. X-ray technology is often used to inspect cargo containers for prohibited items and environmental hazards because it allows for non-destructive and non-invasive visualization, analysis, and inspection. However, traditional X-ray monitoring systems, which acquire radiographs from a single lateral view or occasionally a top view, lack target definition, density, and in-depth spatial information (Moshkbar-Bakhshayesh et al., 2023; Osipov et al., 2020; Valković et al., 2004). Therefore, radiography-based systems are inadequate for inspecting diverse and complex contents of cargo because of the high risk of inter-object occlusion from these viewing directions (Mery et al., 2016; Chen, 2005; Shikhaliev, 2018; Khan et al., 2020; Shao et al., 2022).

Computed tomography (CT) has been used to address the deficiency of radiography-based imaging in 3D localization. By reconstructing high-quality 2D slices and combining multiple slices, CT provides accurate density information through 3D images. A single X-ray source and detector typically rotate together on a circular path around the object to acquire projection data, from a full angular range to allow screeners to identify substances from a wide range of viewpoints. This facilitates resolved imaging of objects that overlap in individual projections, leading to increased detection accuracy compared to single or double-view X-ray radiography (Shikhaliev, 2018; Buser et al., 2020; Petrozziello and Jordanov, 2019; Riffo and Mery, 2012). However, rotation-based CT is time-inefficient, particularly for large cargo volumes, where mechanical limitations of the rotating gantry may result in scan times on the order of hours (Salamon et al., 2025). Static multi-source CT systems eliminate the need for mechanical movement by using multiple fixed X-ray sources to provide multiple viewpoints (Osipov et al., 2020; Neculaes et al., 2014; Gonzales et al., 2013, 2014). This approach enables significantly faster (order of minutes) acquisition with reduced mechanical complexity and lower maintenance demands. Most static CT systems use cold-cathode functional X-ray sources based on field-emitting carbon nanotubes (CNTs) or ZnO nanowires (Gonzales et al., 2014; Wu et al., 2023; Moon et al., 2021; Sugie et al., 2001; Spronk et al., 2021; Duan et al., 2020), which allows for the design of compact and lightweight X-ray setups suitable for inspecting small cargo such as luggage (Neculaes et al., 2014; Gonzales et al., 2013). The X-ray sources consist of linear arrays of fixed focal points that are evenly distributed across the scan volume and fired sequentially or multiplexed

* Corresponding author at: imec-Vision Lab, Department of Physics, University of Antwerp, Antwerp, 2610, Belgium.
E-mail address: caroline.bossuyt@uantwerpen.be (C. Bossuyt).

https://doi.org/10.1016/j.radphyschem.2025.113332
Received 21 December 2024; Received in revised form 7 June 2025; Accepted 21 September 2025
Available online 25 September 2025
0969-806X/© 2025 Published by Elsevier Ltd.

in sets by rapidly switching them on and off, directed at the opposite detector (Neculaes et al., 2014; Gonzales et al., 2013, 2014; Sugie et al., 2001; Spronk et al., 2021; Sprenger et al., 2010). Previous research has demonstrated the functionality of static CT systems, but has not addressed the optimization of the position and orientation of the X-ray sources. For example, Quan and Lalush (2007, 2010) used CNT-based X-ray vacuum tubes to demonstrate the functionality of a rotation-free square and hexagonal micro-CT system through simulations. Gonzales et al. (2013, 2014) investigated the utility of a rectangular acquisition prototype using CNT-based emitters for luggage inspection (<1 m^2), while Spronk et al. (2021) employed such emitters to realize a hexagonal, multi-plane design for stationary head CT. Duan et al. (2020) improved their stacked hexagonal gantry design by using ZnO nanowires for higher density. In a separate study, Masoudi (2019) examined a rectangular system with 25 scattered X-ray sources for inspecting smaller luggage up to 50 cm^2, showing the potential of few-view rectangular designs. Few such studies are available however, and none considered the optimization of rectangular designs for large-scale cargo inspection.

This paper presents a comprehensive framework for evaluation and ultimately optimal design of a multi-source CT system. While our framework can be generalized to other multi-source X-ray configurations, in this work, we focus on a rectangular system design which is the preferred configuration to inspect standard (ISO 668) freight containers. The framework supports positioning and orientation of each X-ray source to maximize the information obtained from the acquired radiographs, as quantified by the Cramér–Rao lower bound (CRLB). It also facilitates targeted inspections of specific regions of interest (ROI), enhancing flexibility and precision. Various source configurations are analyzed and compared using the CRLB-based (ROI) A-optimality criterion. This work lays the foundation for optimizing multi-source CT systems and ultimately improving the efficiency and effectiveness of container inspections.

2. Methods

2.1. System geometry

Fig. 1 illustrates the parametrization of a multi-source CT system with N X-ray sources ($\{s_n\}_{n=1}^N$) that are positioned on a rectangular frame, along with four stationary line detectors placed along the frame's edges. Without loss of generality, we assume the X-ray sources and the centers of the detector elements ($\{d_k\}_{k=1}^K$) to lie in the xy-plane of a global Cartesian coordinate system (x, y, z) positioned at the center of the multi-source system. The position of each X-ray source s_n is parametrized by a (global) angle α_n with respect to the positive x-axis. Its orientation is described by a unit vector $\hat{\boldsymbol{\mu}}_n \in \mathbb{R}^{3\times1}$ defined in a local Cartesian coordinate system (x'_n, y'_n, z'_n), the axes of which are mutually parallel to those of the global coordinate system. The position of each detector element d_k is parametrized by the (global) angle β_k with respect to the positive x-axis, and its orientation by a (local) unit normal vector $\hat{\boldsymbol{n}}_k \in \mathbb{R}^{3\times1}$. All orientation vectors are all assumed to lie in the xy-plane.

2.2. White field intensity distribution

The white field (i.e., the intensity distribution measured by the detector without the presence of the sample) depends on the angular photon emission distribution of the source, the distance from the source to the detector elements, and the orientation of the detector elements. Without loss of generality, the spatial emission distribution of source s_n is assumed to be described by a von Mises–Fisher probability density function centered around s_n:

$$g(\hat{\boldsymbol{t}}|\hat{\boldsymbol{\mu}}_n;\kappa_n) = C(\kappa_n)e^{\kappa_n\hat{\boldsymbol{\mu}}_n^T\hat{\boldsymbol{t}}}, \tag{1}$$

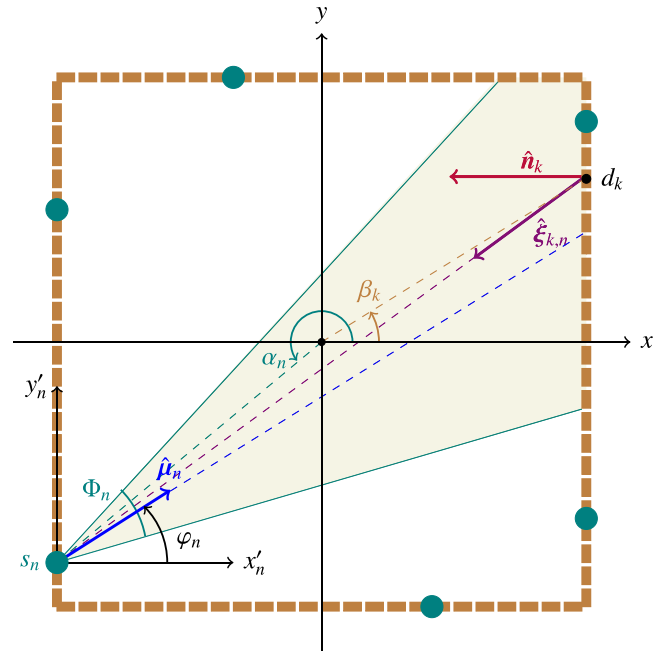

Fig. 1. Parametrization of a rectangular multi-source X-ray system.

with $\hat{\boldsymbol{t}} \in \mathbb{R}^{3\times1}$ a (local) unit vector, $\kappa_n \geq 0$ the so-called concentration parameter, and $C(\kappa_n)$ a normalization constant given by

$$C(\kappa_n) = \frac{\kappa_n}{4\pi \sinh \kappa_n}. \tag{2}$$

Let φ and θ define the azimuthal and polar spherical coordinates (in the local coordinate system of s_n), respectively, such that $\hat{\boldsymbol{t}} = (\sin\theta\cos\varphi, \sin\theta\sin\varphi, \cos\theta)^T$. Furthermore, assume that the source s_n has a fan angle (i.e., azimuthal opening angle) equal to Φ_n and a cone angle (i.e., polar opening angle) equal to Θ_n. Then, the probability $p_{k,n}$ that a photon emitted by the source s_n hits a detector element d_k is given by

$$p_{k,n} = \iint_{S_{k,n}} \text{rect}\left(\frac{\varphi-\varphi_n}{\Phi_n}\right) \text{rect}\left(\frac{\theta-\theta_n}{\Theta_n}\right) g(\hat{\boldsymbol{t}}|\hat{\boldsymbol{\mu}}_n;\kappa_n)\sin\theta d\theta d\varphi, \tag{3}$$

with φ_n and θ_n the spherical coordinates of $\hat{\boldsymbol{\mu}}_n$, $S_{k,n}$ the curved area obtained by projecting the (flat) detector element area S onto the unit sphere ϵ_n centered around s_n, as depicted in Fig. 2, and $rect(\cdot)$ the rectangular function that confines the integration ranges for φ and θ in Eq. (3) to the opening angles Φ_n and Θ_n, respectively. Since the source–detector distance is much larger than the dimension of a detector element, the solid angle subtended by detector element d_k as viewed from source s_n (i.e., $S_{k,n}$) will be small enough to assume the probability density function $g(\hat{\boldsymbol{t}}|\hat{\boldsymbol{\mu}}_n;\kappa_n)$ and rectangular functions to be constant over the range of the integral (cfr. Eq. (3)). This means that Eq. (3) can be approximated as:

$$p_{k,n} \approx \text{rect}\left(\frac{\varphi_{k,n}-\varphi_n}{\Phi_n}\right) \text{rect}\left(\frac{\theta_{k,n}-\theta_n}{\Theta_n}\right) g(\hat{\boldsymbol{t}}_{k,n}|\hat{\boldsymbol{\mu}}_n;\kappa_n)\, S\, \frac{\hat{\boldsymbol{n}}_k^T\hat{\boldsymbol{\xi}}_{k,n}}{r_{k,n}^2}, \tag{4}$$

with $\hat{\boldsymbol{t}}_{k,n} = (\sin\theta_{k,n}\cos\varphi_{k,n}, \sin\theta_{k,n}\sin\varphi_{k,n}, \cos\theta_{k,n})^T$, where $\varphi_{k,n}$ and $\theta_{k,n}$ denote the azimuthal and polar spherical coordinates of detector element d_k in the local coordinate system of s_n, respectively, $\hat{\boldsymbol{\xi}}_{k,n} \in \mathbb{R}^{3\times1}$ represents the (local) unit vector emanating from d_k towards s_n (cfr. Fig. 1), and $r_{k,n}$ is the distance between s_n and d_k. Finally, if the number of photons emitted per second by the X-ray source is given by J_0, then the expected number of photons per second detected by detector element d_k is given by

$$I_{0,k,n} = J_0 p_{k,n}. \tag{5}$$

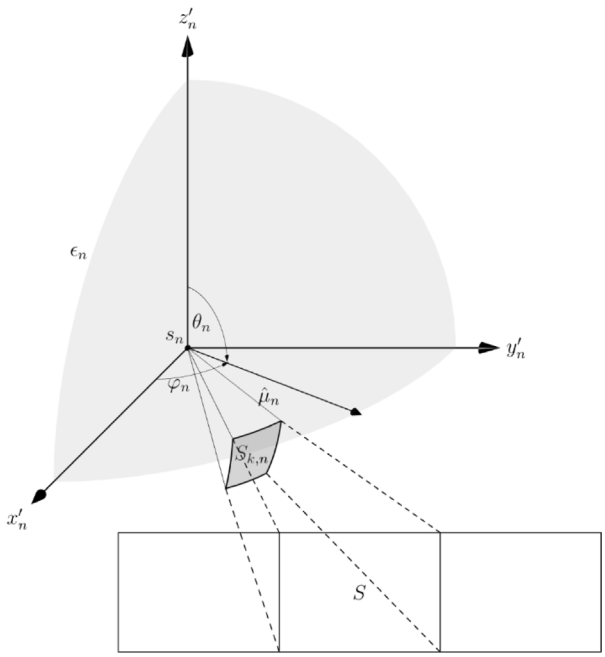

Fig. 2. Projection of detector element d_k with flat surface area S onto the unit sphere ϵ_n in the reference frame of the X-ray source (s_n), yielding the projected detector element with a curved surface area $S_{k,n}$.

2.3. Object-induced intensity distribution

In what follows, the object slice to be scanned is assumed to be discretized on a 2D rectangular grid of V voxels (cfr. Fig. 3) and represented as $\boldsymbol{x} = (x_v) \in \mathbb{R}^{V\times 1}$. The expected number of photons $\lambda_{k,n}$ (per second) detected by d_k can then be described by the Lambert–Beer model as

$$\lambda_{k,n} = I_{0,k,n} e^{-\boldsymbol{w}_{k,n}^T \boldsymbol{x}}, \tag{6}$$

where $\boldsymbol{w}_{k,n} = (w_{k,n,v}) \in \mathbb{R}^{V\times 1}$ is a vector representing the contributions of the individual object voxel values to $\lambda_{k,n}$. In this work, these contributions are assumed to correspond with the length of the intersection between the object voxel and the line that connects source s_n with the center of detector element d_k (cfr. Fig. 3).

2.4. Statistical experiment design

In this work, intensity measurements at the detector elements, called observations, are photon counts that fluctuate randomly about their expected values and can be modeled as Poisson distributed random variables, denoted as $\underline{I}_{k,n}$. Without loss of generality, the expected values of $\underline{I}_{k,n}$ are assumed to be equal to $\lambda_{k,n}$ (cfr. Eq. (6)), i.e.,

$$\mathbb{E}[\underline{I}_{k,n}] = \lambda_{k,n} = \eta_{k,n}(\boldsymbol{x}|\beta_k, \hat{\boldsymbol{n}}_k, \alpha_n, \hat{\boldsymbol{\mu}}_n, \boldsymbol{\Phi}_n, \boldsymbol{\Theta}_n, J_0, \kappa_n), \tag{7}$$

where $\mathbb{E}[\cdot]$ denotes the expectation operator and $\eta_{k,n}(\cdot)$ represents the expectation model that depends on the parameters $\boldsymbol{x}$ that define the object, as well as on the system parameters β_k, $\hat{\boldsymbol{n}}_k$, α_n, $\hat{\boldsymbol{\mu}}_n$, $\boldsymbol{\Phi}_n$, $\boldsymbol{\Theta}_n$, J_0, and κ_n as described by Eqs. (1)–(6). The probability that the Poisson distributed observation $\underline{I}_{k,n}$ is equal to $I_{k,n}$, with $I_{k,n}$ the independent variable corresponding to $\underline{I}_{k,n}$, is given by

$$\frac{\lambda_{k,n}^{I_{k,n}} e^{-\lambda_{k,n}}}{I_{k,n}!}. \tag{8}$$

If the observations are assumed to be statistically independent, the probability that the set of observations $\underline{\boldsymbol{I}} = (\underline{I}_{1,1}, \underline{I}_{1,2}, \dots, \underline{I}_{K,N})^T$ is equal to $\boldsymbol{I} = (I_{1,1}, I_{1,2}, \dots, I_{K,N})^T$ is given by:

$$P(\boldsymbol{I}|\boldsymbol{x}) = \prod_{n=1}^{N}\prod_{k=1}^{K} \frac{\lambda_{k,n}^{I_{k,n}} e^{-\lambda_{k,n}}}{I_{k,n}!}. \tag{9}$$

This function is called the joint probability function (PF) of the observations. Note that the object parameters as well as the system parameters enter the joint PF via $\lambda_{k,n}$. When determining the PF, the system parameters are assumed to be known, whereas $\boldsymbol{x}$ is the unknown parameter vector to be estimated. It can be shown that the covariance matrix of any unbiased estimator $\hat{\boldsymbol{x}}$ of $\boldsymbol{x}$, i.e. $\mathrm{cov}(\hat{\boldsymbol{x}})$, satisfies:

$$\mathrm{cov}(\hat{\boldsymbol{x}}) \geq \boldsymbol{F}^{-1}, \tag{10}$$

where $\boldsymbol{F} \in \mathbb{R}^{V\times V}$ is the Fisher information matrix (FIM) defined as

$$\boldsymbol{F} = -\mathbb{E}\left[\frac{\delta^2 \ln P(\underline{\boldsymbol{I}}|\boldsymbol{x})}{\delta \boldsymbol{x} \delta \boldsymbol{x}^T}\right]. \tag{11}$$

Straightforward calculations show that $\boldsymbol{F}$ can be expressed as

$$\boldsymbol{F} = \boldsymbol{W}^T \mathrm{diag}\left(\boldsymbol{I}_0 \circ e^{-\boldsymbol{W}\boldsymbol{x}}\right) \boldsymbol{W}, \tag{12}$$

with $\boldsymbol{W} \in \mathbb{R}^{(KN)\times V}$ the projection matrix obtained by stacking all row vectors $\{\boldsymbol{w}_{k,n}^T\}$, and where $\circ$ denotes the Hadamard product (Masoudi, 2019). Since the diagonal elements of $\mathrm{cov}(\hat{\boldsymbol{x}})$ represent the variances of $\hat{x}_1, \dots, \hat{x}_V$ and the diagonal elements of a positive semi-definite matrix are non-negative, it follows from Eq. (10) that:

$$\mathrm{var}(\hat{x}_v) \geq (\boldsymbol{F}^{-1})_{vv}, \tag{13}$$

where $v = 1, \dots, V$ and $(\boldsymbol{F}^{-1})_{vv}$ is the (v,v)th element of the inverse of the FIM. The matrix $\boldsymbol{F}^{-1}$ is known as the Cramér–Rao Lower Bound (CRLB) matrix and its diagonal elements are known as the Cramér–Rao (CR) variances (van den Bos, 2007). Hence, it follows from Eq. (13) that the CRLB provides a theoretical lower bound on the variance with which the parameters $\boldsymbol{x}$ can be estimated unbiasedly from noise disturbed measurements $\underline{\boldsymbol{I}}$. As such, the CRLB inherently accounts for the effect of noise on the estimation precision. Furthermore, since the joint PF (Eq. (9)) is a function of the system parameters, of which some are tunable (e.g., the positions and orientations of the X-ray sources), the CRLB matrix is a function of these parameters as well. Therefore, the CRLB can be used to evaluate and optimize the experiment design in terms of precision (i.e., variance). For this purpose, optimality criteria can be applied as scalar functions of the CRLB elements. In this paper, we apply the A-optimality criterion defined as

$$\mathrm{tr}(\boldsymbol{F}^{-1}), \tag{14}$$

which involves summing of the CR variances. Alternatively, when focusing on a ROI, the ROI A-optimality criterion will be applied, which we define as:

$$\sum_{v\in\mathcal{T}} (\boldsymbol{F}^{-1})_{vv}, \tag{15}$$

where the subset $\mathcal{T}$ corresponds with the voxels within the ROI.

2.5. Maximum likelihood estimator

The guiding principle behind CRLB based statistical experiment design is the assumption that an estimator exists that attains the CRLB (van den Bos, 2007). The maximum likelihood estimator (MLE) is known to attain this bound at least asymptotically. It is obtained by maximizing the likelihood function, which is closely related to the joint PF (cfr. Eq. (9)). While the joint PF is a function of the observations for a given value of the parameters, the likelihood function is a function of the parameters for a given set of observations. Hence, the MLE $\hat{\boldsymbol{x}}_{\mathrm{ML}}$ of $\boldsymbol{x}$ can be expressed as

$$\hat{\boldsymbol{x}}_{\mathrm{ML}} = \arg\max_{\boldsymbol{x}} P(\underline{\boldsymbol{I}}|\boldsymbol{x}). \tag{16}$$

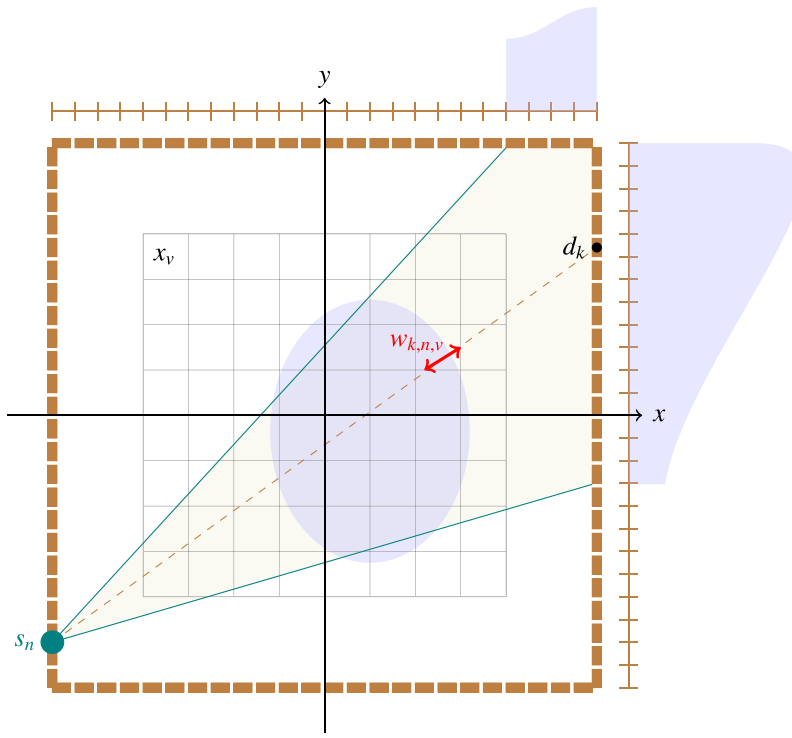

Fig. 3. The X-ray projection geometry for a single X-ray source in a rectangular CT system applied to an object discretized on a 2D rectangular voxel grid.

From Eqs. (7), (9), and (16), we obtain

$$\hat{\boldsymbol{x}}_{\mathrm{ML}} = \arg\max_{\boldsymbol{x}} \sum_{n=1}^{N}\sum_{k=1}^{K}(-\eta_{k,n}(\boldsymbol{x}) + \underline{I}_{k,n}\ln\eta_{k,n}(\boldsymbol{x}))\,, \tag{17}$$

where, for simplicity, the dependence of the expectation model $\eta_{k,n}(\cdot)$ on the system parameters has been omitted in the notation. Using Eqs. (6) and (7), Eq. (17) simplifies to

$$\hat{\boldsymbol{x}}_{\mathrm{ML}} = \arg\min_{\boldsymbol{x}} \sum_{n=1}^{N}\sum_{k=1}^{K}(I_{0,k,n}e^{-\boldsymbol{w}_{k,n}^T\boldsymbol{x}} + \underline{I}_{k,n}\boldsymbol{w}_{k,n}^T\boldsymbol{x})\,. \tag{18}$$

Under general conditions, the MLE is known to be consistent and asymptotically efficient and unbiased (van den Bos, 2007). This means that the probability density function of the MLE tends asymptotically to a normal probability density function with the true parameter values as expectations and the CRLB as covariance matrix. If this asymptotic property of the MLE also applies for a finite number of observations will be investigated in simulations.

3. Experiments

Simulation experiments were set up to validate the proposed framework for statistical experiment design of a multi-source rectangular X-ray cargo scanning system. First, to justify the use of the A-optimality criterion for experiment design, simulation experiments were performed to verify that the MLE indeed attains the CRLB (cfr. Section 3.1). Next, in Section 3.2, different source configurations are evaluated and compared in terms of the (ROI) A-optimality criterion.

All experiments and evaluations were based on the rectangular CT setup described in Section 2.1, using the ASTRA Toolbox (Van Aarle et al., 2016). Each of the four detectors of length $L = 3\,\mathrm{m}$ comprised 3000 square detector elements of size $l = 1\,\mathrm{mm}$. The polar and azimuthal opening angles of the X-ray sources were set to $\Theta_n = 3.5°$ and $\Phi_n = 60°$, respectively. Without loss of generality, the concentration parameters κ_n (Eq. (2)) were set to 15 and the energy of each X-ray source to 8 MeV. Furthermore, J_0 was set such that 10^{10} photons/s were emitted within the opening angle of the X-ray source, and with an exposure time of 1 s (Rogers et al., 2017). Objects were represented on a 50 × 50 voxel grid, covering a 1 m × 1 m reconstruction area (RA), positioned in the center of the multi-source system.

Three phantoms were used in the experiments: a numerical container (NC) phantom (Fig. 4(a)), an experimental container (EC) phantom (Fig. 4(b)), and a Shepp–Logan (SL) phantom (Fig. 4(c)). The NC phantom consisted of a 2 mm thick container wall of weathering steel (Corten B) filled with cocaine hydrochloride ($C_{17}H_{21}NO_4 \cdot HCl$) at 8 MeV. The EC phantom was based on a high-quality image obtained by applying a gradient descent-based reconstruction method (Barzilai and Borwein, 1988) to experimental data consisting of 1440 projections, originally acquired in a circular fan beam geometry at XXL-CT at Fraunhofer EZRT (Salamon et al., 2016). The SL phantom had the same attenuation range as the EC phantom (0–$10^{-3}\,\mathrm{mm}^{-1}$) and was used to evaluate the (ROI) A-optimality criterion for different phantoms but with similar attenuation distributions.

3.1. Attaining the CRLB with ML estimation

In this section, we aim to justify the use of the A-optimality criterion (Eq. (14)) to evaluate and compare the design of rectangular multi-source X-ray systems. To that end, simulation experiments were performed to verify if there exists an estimator that attains the CRLB. Although the MLE derived in Section 2.5 is known to have this property at least asymptotically, simulation experiments are required to ascertain its behavior for a finite number of observations. Hence, Monte Carlo (MC) simulations experiments were conducted using the NC phantom for a small but representative set of configurations of the multi-source X-ray system, where the number, positions, and orientations of the X-ray sources varied across the configurations, as presented in Table 1. The sources, with $\alpha_1 = 0°$, were either evenly spaced along the frame (*equidistant*) or equiangularly distributed (*equiangular*). Fig. 5(b) illustrates the equidistant and equiangular distributions for $N = 24$. Finally, in all considered configurations (cfr. Table 1), the sources were either oriented towards the *center* of the reconstruction grid or to the center of the bottom-left quadrant (*corner*) of the grid, as illustrated in Figs. 5(b) and 5(d), respectively.

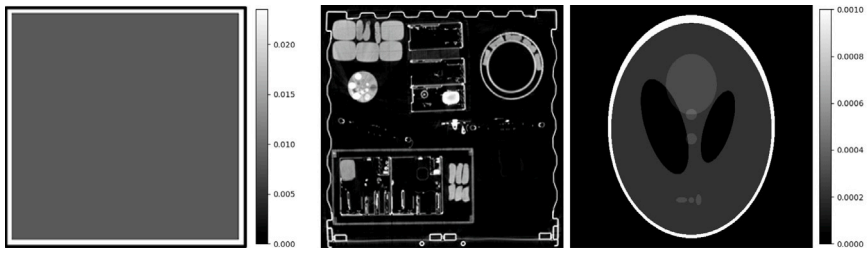

(a) NC (b) EC (c) SL

Fig. 4. (a) The NC, (b) EC, and (c) SL phantoms.

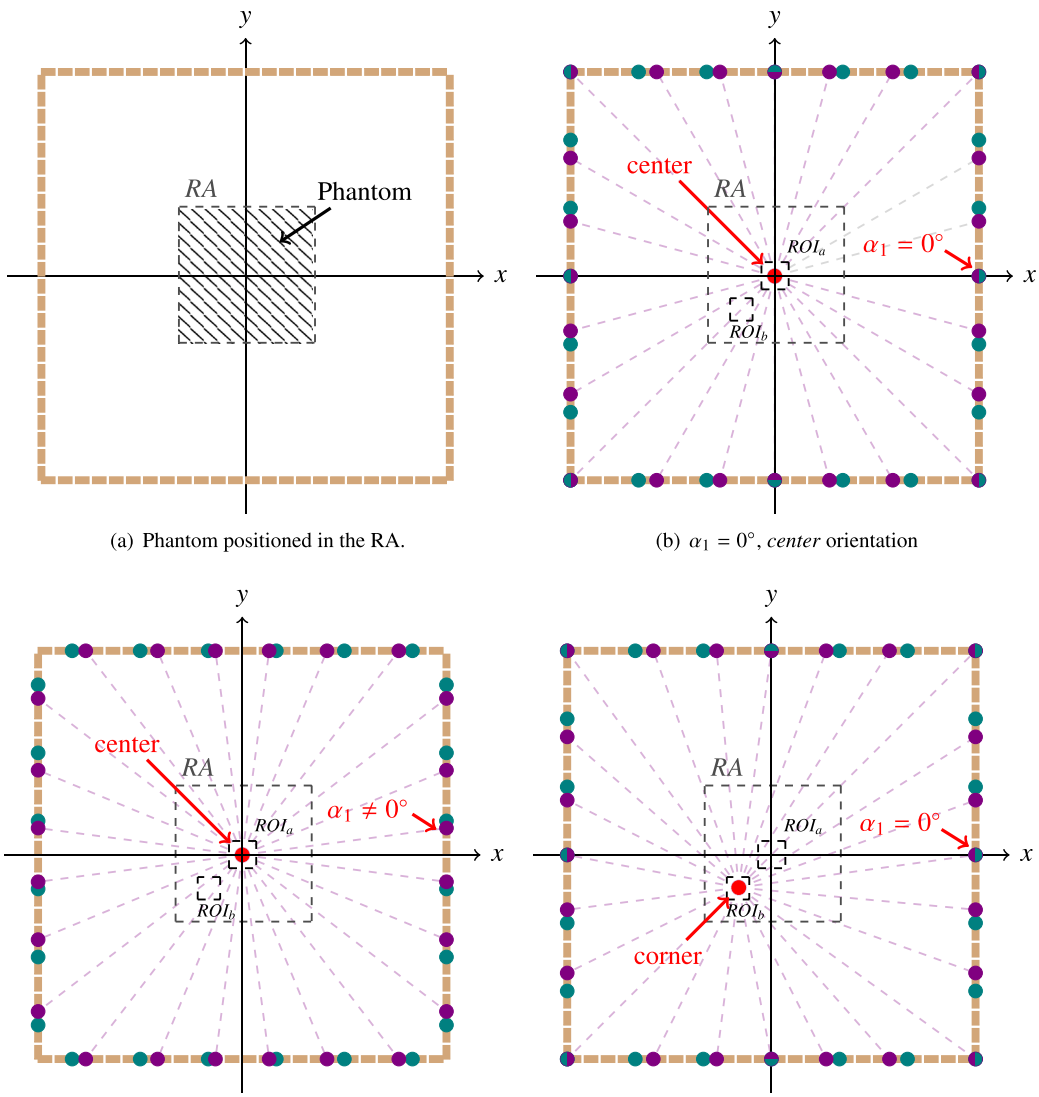

(a) Phantom positioned in the RA.

(b) $\alpha_1 = 0°$, *center* orientation

(c) $\alpha_1 \neq 0°$, *center* orientation

(d) $\alpha_1 = 0°$, *corner* orientation

Fig. 5. (a) A phantom positioned in the center of the rectangular CT system. (b) Equidistant (teal) and equiangular (purple) configurations with $N = 24$ sources and zero offset ($\alpha_1 = 0°$), oriented towards the center of the RA (cfr. ROI_a). (c) The same configuration as in (b) but with a non-zero offset ($\alpha_1 \neq 0$). (d) Zero offset ($\alpha_1 = 0°$), with sources oriented towards the center of the bottom-left quadrant (corner) of the RA (cfr. ROI_b).

For each experiment, $U = 50$ noise realizations of Poisson distributed intensity measurements were generated using the forward model described in Section 2. For each noise realization, the object was reconstructed with the MLE described by Eq. (18), starting in $\boldsymbol{x} = \mathbf{0}$, which yielded a sample of U ML estimates for each voxel. From these samples, $100(1-\alpha)\%$ confidence intervals with significance level $\alpha = 0.05$ were calculated for the mean $\mu_{\text{ML},v}$ and variance $\sigma^2_{\text{ML},v}$ of the MLE in each voxel as (Mood et al., 1974)

$$\left[\overline{\{\hat{x}_{\text{ML},v,u}\}_{u=1}^{U}} - t_{\frac{\alpha}{2},U-1}\frac{S_v}{\sqrt{U}}, \overline{\{\hat{x}_{\text{ML},v,u}\}_{u=1}^{U}} + t_{\frac{\alpha}{2},U-1}\frac{S_v}{\sqrt{U}}\right] \tag{19}$$

and

$$\left[\frac{(U-1)S_v^2}{\chi^2_{\frac{\alpha}{2},U-1}}, \frac{(U-1)S_v^2}{\chi^2_{1-\frac{\alpha}{2},U-1}}\right], \tag{20}$$

respectively, with $\overline{\{\hat{x}_{\mathrm{ML},v,u}\}_{u=1}^{U}}$ and S_v the voxel-wise sample mean and sample standard deviation, respectively, $t_{\frac{\alpha}{2},U-1}$ the $100(1-\frac{\alpha}{2})$%-percentile of a t-distributed random variable with $(U-1)$ degrees of freedom, and $\chi^2_{\frac{\alpha}{2},U-1}$ the $100(1-\frac{\alpha}{2})$%-percentile of a χ^2-distributed random variable with $(U-1)$ degrees of freedom. Next, the null hypothesis $H_{0,\mathrm{bias}}$ that the MLE $\hat{x}_{\mathrm{ML},v}$ is unbiased was rejected at the significance level α if the confidence interval for $\mu_{\mathrm{ML},v}$ did not contain the ground truth parameter x_v. Similarly, the null hypothesis $H_{0,\mathrm{var}}$ that the variance of $\hat{x}_{\mathrm{ML},v}$ equals the corresponding CR variance was rejected at the significance level α if the confidence interval for $\sigma^2_{\mathrm{ML},v}$ did not contain the corresponding CR variance.

3.2. Statistical experiment design

To demonstrate the effectiveness of our proposed framework for experiment design in rectangular multi-source X-ray systems, various source configurations were compared in terms of the (ROI) A-optimality criterion. To this end, the A-optimality criterion was computed across the RA, while the ROI A-optimality criterion was computed for two ROIs of 10×10 voxels. The first region, ROI_a, was centered within the RA, while the second region, ROI_b, was positioned in the bottom-left quadrant (corner) of the RA. Furthermore, relative (ROI) A-efficiencies were computed, where the relative A-efficiency between two configurations characterized by the FIMs $\boldsymbol{F}_1$ and $\boldsymbol{F}_2$ is defined as (Jones et al., 2021):

$$\frac{\mathrm{tr}(\boldsymbol{F}_2^{-1})}{\mathrm{tr}(\boldsymbol{F}_1^{-1})}. \tag{21}$$

Similarly to Eq. (15), we define the relative ROI A-efficiency as:

$$\frac{\sum_{v\in\mathcal{T}}(\boldsymbol{F}_2^{-1})_{vv}}{\sum_{v\in\mathcal{T}}(\boldsymbol{F}_1^{-1})_{vv}}. \tag{22}$$

Since the (ROI) A-optimality criterion is a measure of the attainable precision, with lower values corresponding to a higher precision, a relative (ROI) A-efficiency greater than one indicates that the first configuration provides a higher attainable precision than the second. While the (ROI) A-optimality criterion and relative (ROI) A-efficiency provide concise, single-value metrics for comparing estimation precision across configurations, CR variance maps offer a complementary, voxel-level visualization of attainable precision.

First, a set of configurations was compared in terms of the (ROI) A-optimality criterion using the NC, EC, and SL phantoms, in which the sources were arranged either equidistantly ($\boldsymbol{F}_2$) along the rectangular frame or equiangularly ($\boldsymbol{F}_1$). This comparison was carried out for $N = 24, 36$, and 48 X-ray sources, with N chosen to reflect realistic scenarios in cargo container inspection (Masoudi et al., 2016). Additionally, the effect of increased sampling density was investigated by extending the comparison to configurations with increments of 12 sources, from $N = 24$ up to 96. To compare the equiangular and equidistant configurations (for an equal number of sources) independent of the offset, the (ROI) A-optimality criteria were averaged across 15 offsets. For the equiangular configuration, these offsets corresponded with 15 equiangular substeps within the range from $\alpha_1 = 0°$ to $\alpha_1 = \left(\frac{360}{N}\right)^{\circ}$, whereas subsampling with 15 equidistant substeps was applied to define the 15 offsets for the equidistant configuration. In both cases, for all offsets, the sources were oriented either towards the center of the X-ray system (Fig. 5(b)), in line with conventional approaches, or towards the center of the bottom-left quadrant (corner) of the phantom (Fig. 5(d)). Next, the same set of configurations was compared in terms of the relative (ROI) A-efficiency, with the (ROI) A-optimality criteria averaged over 15 offsets before calculating the relative (ROI) A-efficiency for each configuration. Finally, difference maps of the offset-invariant CR variances for the NC phantom were computed for both equidistant and equiangular source distributions with $N = 24, 48$, and 96 sources, comparing systems with corner-oriented sources (cfr. Fig. 5(d)) to those with center-oriented sources (cfr. Fig. 5(b)).

Table 1
Percentage of phantom voxels for which the null hypotheses that the MLE is unbiased ($H_{0,\mathrm{bias}}$) and attains the CRLB ($H_{0,\mathrm{var}}$) were not rejected (at significance level 0.05).

N	Positions ($\alpha_1 = 0°$)	Orientation	$H_{0,\mathrm{var}}$ (%)	$H_{0,\mathrm{bias}}$ (%)
24	Equidistant	Center	95.7	98.2
36	Equidistant	Center	94.0	97.4
48	Equidistant	Center	95.5	95.4
36	Equidistant	Corner	95.8	94.5
36	Equiangular	Center	95.2	95.6

4. Results and discussions

4.1. Attaining the CRLB with ML estimation

Table 1 presents the percentage of voxels for which the null hypotheses $H_{0,\mathrm{var}}$ and $H_{0,\mathrm{bias}}$ were not rejected at significance level 0.05 for different configurations of the rectangular multi-source X-ray system. Results are shown for various configurations of the rectangular multi-source X-ray system, indicated by the number of X-ray sources (N), their positions (equidistant or equiangular), and joint orientation. These results indicate that in approximately 95% of the voxels the hypotheses that the MLE is unbiased and attains the CRLB were not rejected at significance level 0.05. This supports the use of the CRLB as performance measure for optimal experiment design in this work.

4.2. Statistical experiment design

Fig. 6 shows the offset-invariant (ROI) A-optimality values as a function of the number of X-ray sources, evaluated in the RA (Fig. 6(a)), ROI_a (Fig. 6(b)), and ROI_b (Fig. 6(c)). This dependency is shown for equiangular and equidistant source distributions with center and corner orientations, applied to the NC, EC, and SL phantoms. The SL and EC phantoms consistently yield nearly identical (ROI) A-optimality values due to their similar ranges of attenuation coefficients. The significant difference – approximately an order of magnitude – between the (ROI) A-optimality values of the NC phantom and those of the SL and EC phantoms can be attributed to their respective attenuation coefficient ranges. Specifically, the average attenuation coefficient of the NC phantom is approximately 20 times higher than those of the SL and EC phantoms, resulting in a reduced photon count and consequently a lower precision. The differences in A-optimality between the RA and the ROIs shown in Fig. 6 are mainly due to the varying number of voxels. Additionally, Figs. 6(a) and 6(b) reveal that, for both the RA and ROI_a, center-oriented configurations yield lower (ROI) A-optimality values compared to corner-oriented configurations. In contrast, Fig. 6(c) shows that, for ROI_b, corner-oriented configurations outperform center-oriented configurations in terms of ROI A-optimality. This suggests that to achieve optimal overall precision across the RA, the sources should be oriented towards the center. However, to maximize precision within a specific ROI (either ROI_a or ROI_b), the sources should be oriented towards the center of that ROI. The (ROI) A-optimality trends are consistent across phantoms.

Table 2 presents the offset-invariant relative (ROI) A-efficiencies for center-oriented (cfr. Part 1) and corner-oriented (cfr. Part 2) configurations as a function of the number of X-ray sources, evaluated for the NC, EC, and SL phantoms across the RA, ROI_a, and ROI_b. The relative (ROI) A-efficiency values greater than one indicate that equiangular

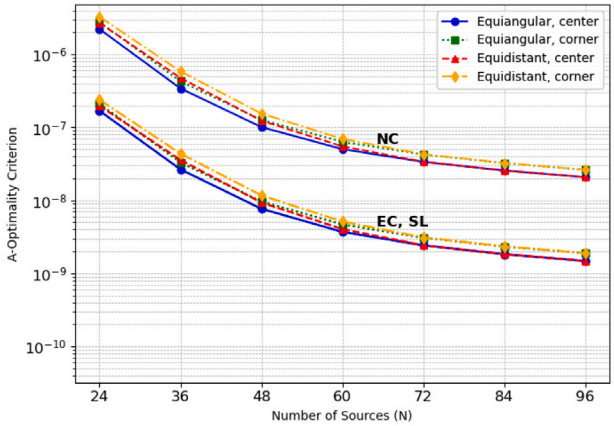

(a) RA

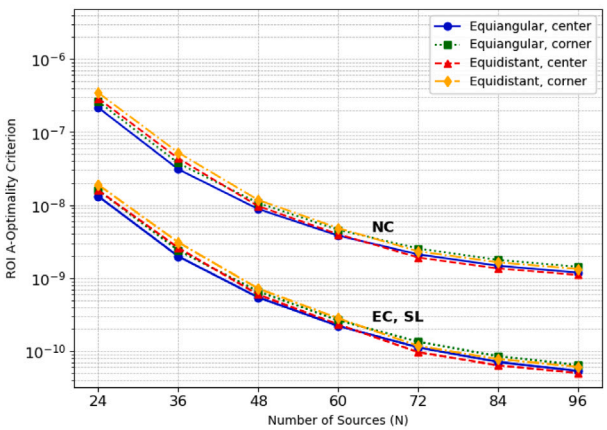

(b) ROI_a

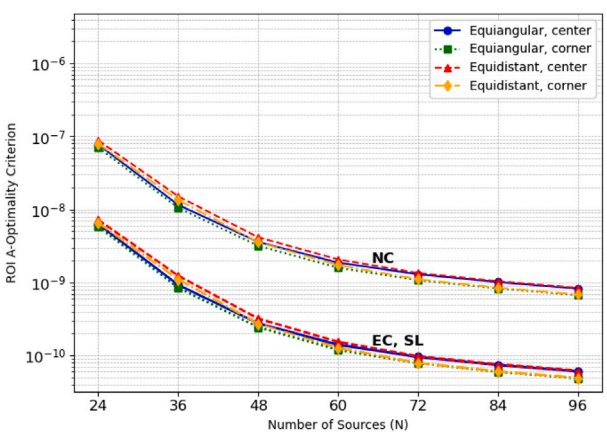

(c) ROI_b

Fig. 6. Offset-invariant (ROI) A-optimality criterion as a function of N in the RA (a), ROI_a (b), and ROI_b (c) for the NC, EC, and SL phantoms. The sources are distributed equidistantly or equiangularly, with orientations either towards the center or corner of the RA.

configurations outperform equidistant ones in estimation precision, even though equiangular configurations have approximately 1% fewer observations (i.e., measurements at detector elements). However, as can be seen from Table 2, for large numbers of X-ray sources ($N > 60$), the relative (ROI) A-optimality criterion approaches 1, indicating that the equiangular and equidistant configurations provide comparable Fisher information.

Table 2
Offset-invariant relative (ROI) A-efficiency values for N X-ray sources are evaluated within the RA, ROI_a, and ROI_b across the NC, EC, and SL phantoms.

N	Offset-invariant relative (ROI) A-efficiency								
	NC			EC			SL		
	RA	ROI_a	ROI_b	RA	ROI_a	ROI_b	RA	ROI_a	ROI_b
Part 1: orientation *center*									
24	1.22	1.34	1.14	1.17	1.21	1.14	1.16	1.21	1.14
36	1.40	1.41	1.31	1.35	1.31	1.34	1.35	1.31	1.34
48	1.22	1.10	1.16	1.22	1.09	1.17	1.22	1.10	1.17
60	1.10	1.05	1.11	1.09	1.04	1.10	1.09	1.05	1.10
72	1.01	0.91	1.04	1.00	0.86	1.03	1.00	0.87	1.02
84	1.00	0.92	1.03	1.00	0.90	1.03	1.00	0.90	1.03
96	1.00	0.93	1.03	1.00	0.93	1.02	1.01	0.92	1.02
Part 2: orientation *corner*									
24	1.19	1.32	1.13	1.14	1.20	1.13	1.14	1.19	1.13
36	1.37	1.39	1.28	1.32	1.29	1.31	1.32	1.29	1.31
48	1.22	1.10	1.12	1.21	1.10	1.12	1.22	1.10	1.12
60	1.10	1.06	1.09	1.10	1.06	1.07	1.10	1.07	1.07
72	1.01	0.92	1.03	1.01	0.87	1.01	1.01	0.88	1.01
84	1.01	0.93	1.02	1.01	0.91	1.02	1.01	0.92	1.02
96	1.01	0.93	1.02	1.00	0.94	1.02	1.01	0.95	1.02

Fig. 7 shows the difference maps of the offset-invariant CR variances for the NC phantom, comparing two system configurations: one with corner-oriented sources (as shown in Fig. 5(d)) and the other with center-oriented sources (as depicted in Fig. 5(b)) for $N = 24$, 48, and 96. These maps show the variance differences between corner- and center-oriented sources, with negative values indicating lower variances for the corner-oriented system, and positive values indicating lower variances for the center-oriented system. It can be observed from Fig. 7 that in and around the corner region, the corner-oriented configuration provides a higher precision than the center-oriented configuration, whereas outside this region the center-oriented configuration performs better (in terms of precision), confirming that it pays off to orient the sources to the target ROI. Additionally, Fig. 7 shows that as the number of sources increases, the CR variance patterns associated with both configurations tend to converge to one another.

4.3. Experiment design considerations

A key consideration in system design is the trade-off between scanning time and imaging precision. Longer scans typically improve the signal-to-noise ratio (SNR) by increasing the number of detected photons, thereby reducing the CR variances. However, our results demonstrate that precision can also be significantly improved through the optimization of source configurations. This suggests that careful experiment design may serve as a viable alternative to longer acquisition times, and in some cases, allow for faster scanning without compromising reconstruction quality. The present study assumes a planar design for the rectangular multi-source and multi-detector CT system, which simplifies the analysis and enables a focused investigation of the core optimization principles. While this abstraction omits certain engineering aspects, such as shielding requirements, limits on source power, and restrictions on beam angles, it does not restrict the generality of the framework, which can be readily extended to non-planar configurations through appropriate adaptations of the system model. In addition, the proposed framework is not restricted to the rectangular system geometry explored here. The methodology can be applied to alternative layouts, such as circular, hexagonal, or even irregular designs, by redefining source and detector placements. Future work will focus on optimizing configurations by refining source positioning and orientation based on CR variances, evaluating the impact of sources with varying peak energies, and improving detector characteristics to enhance system performance.

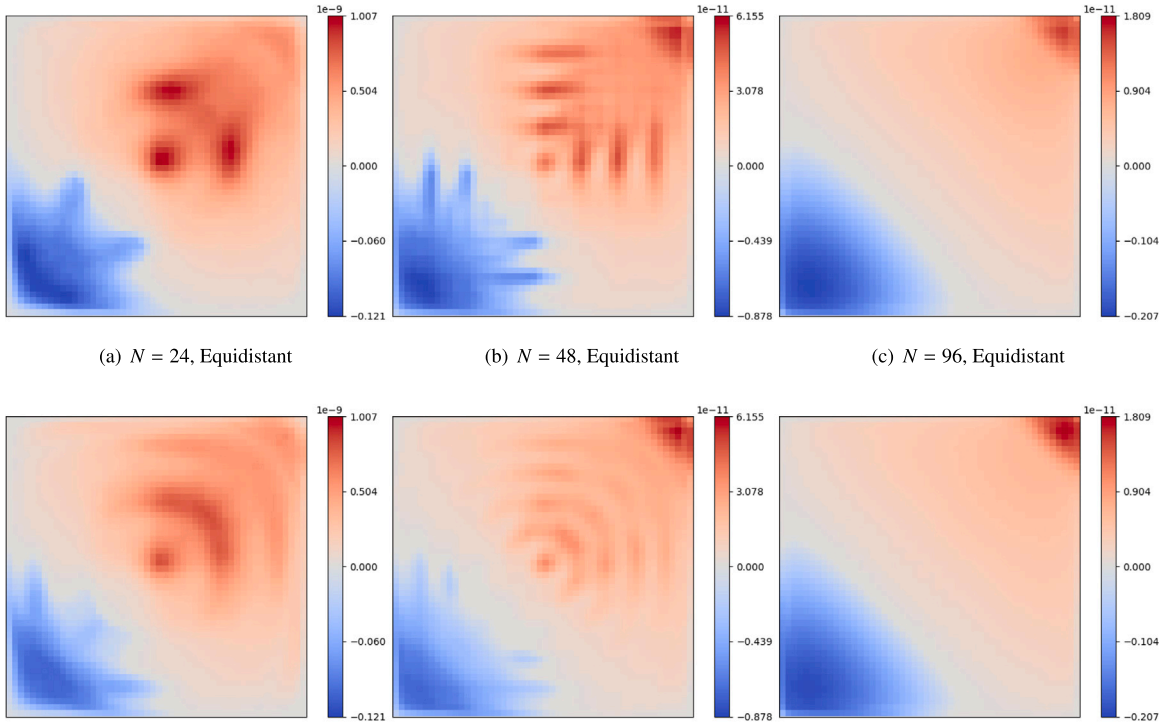

(a) $N = 24$, Equidistant (b) $N = 48$, Equidistant (c) $N = 96$, Equidistant

(d) $N = 24$, Equiangular (e) $N = 48$, Equiangular (f) $N = 96$, Equiangular

Fig. 7. Difference maps of the offset-invariant Cramér–Rao variances of the NC phantom for a system with corner-oriented sources (cfr. Fig. 5(d)) and a system with center-oriented sources (cfr. Fig. 5(b)). Results are shown for N equidistantly (a–c) or equiangularly (d–f) distributed sources.

5. Conclusions

A framework was presented for experiment design of a rectangular multi-source X-ray CT cargo scanning system. The potential of the framework was illustrated by a comprehensive evaluation of different source configurations, varying the number, distribution, and orientation of the X-ray sources, where the CRLB-based A-optimality criterion was proposed as a performance measure. This evaluation highlighted the importance of source positioning and orientation in optimizing imaging precision. Specifically, the relative A-efficiencies demonstrated that equiangular configurations outperform equidistant ones in terms of estimation precision, especially for relatively low numbers of X-ray sources. Furthermore, experiments showed that the optimal configuration depends on the ROI being imaged. While the results presented in this paper are not directly applicable to non-rectangular system configurations, the underlying framework is transferable to more complex geometries.

The proposed framework lays the foundation for future work involving more realistic source and detector models, as well as validation with experimental data, and steps towards translating this work to practical system design and optimization.

CRediT authorship contribution statement

Caroline Bossuyt: Writing – original draft, Writing – review & editing, Software, Visualization, Investigation, Data curation, Validation, Methodology, Formal analysis, Conceptualization. **Arnold J. den Dekker:** Writing – review & editing, Conceptualization, Supervision, Methodology, Writing – original draft. **Domenico Iuso:** Software, Writing – review & editing, Data curation, Investigation. **Jan De Beenhouwer:** Methodology, Writing – review & editing, Conceptualization, Writing – review & editing, Supervision, Funding acquisition. **Jan Sijbers:** Writing – review & editing, Supervision, Conceptualization, Writing – review & editing, Project administration, Methodology, Funding acquisition.

Declaration of competing interest

The authors declare that they have no known competing financial interests or personal relationships that could have appeared to influence the work reported in this paper.

Acknowledgments

The authors have received funding from the European Union's Horizon 2020 research and innovation programme under grant agreement No 101020100 as well as from Fonds voor Wetenschappelijk Onderzoek Vlaanderen (G090020N, G094320N, S003421N).

Appendix A. Supplementary data

Supplementary material related to this article can be found online at https://doi.org/10.1016/j.radphyschem.2025.113332.

Data availability

Data will be made available on request.

References

Barzilai, J., Borwein, J.M., 1988. Two-point step size gradient methods. IMA J. Numer. Anal. 8 (1), 141–148.

Buser, D., Sterchi, Y., Schwaninger, A., 2020. Why stop after 20 minutes? Breaks and target prevalence in a 60-minute X-ray baggage screening task. Int. J. Ind. Ergon. 76, 102897.

Chen, G., 2005. Understanding X-ray cargo imaging. Nucl. Instrum. Methods Phys. Res. Sect. B: Beam Interact. Mater. Atoms 241 (1–4), 810–815.

Duan, Y., Cheng, H., Wang, K., Mou, X., 2020. A novel stationary CT scheme based on high-density X-ray sources device. IEEE Access 8, 112910–112921.

Gonzales, B., Spronk, D., Cheng, Y., Tucker, A.W., Beckman, M., Zhou, O., Lu, J., 2014. Rectangular fixed-gantry CT prototype: combining CNT X-ray sources and accelerated compressed sensing-based reconstruction. IEEE Access 2, 971–981.

Gonzales, B., Spronk, D., Cheng, Y., Zhang, Z., Pan, X., Beckmann, M., Zhou, O., Lu, J., 2013. Rectangular computed tomography using a stationary array of CNT emitters: Initial experimental results. In: Medical Imaging 2013: Physics of Medical Imaging. Vol. 8668, SPIE, pp. 1450–1457.

Jones, B., Allen-Moyer, K., Goos, P., 2021. A-optimal versus D-optimal design of screening experiments. J. Qual. Technol. 53 (4), 369–382.

Khan, S.U., Khan, I.U., Ullah, I., Saif, N., Ullah, I., 2020. A review of airport dual energy X-ray baggage inspection techniques: Image enhancement and noise reduction. J. X-Ray Sci. Technol. 28 (3), 481–505.

Masoudi, A., 2019. Task-Based Information-Theoretic Design of X-Ray Computed Tomography Systems: Detection and Estimation Tasks (Ph.D. thesis). The University of Arizona.

Masoudi, A., Thamvichai, R., Neifeld, M.A., 2016. Computed tomography imaging system design for shape threat detection. Opt. Eng., Bellingham 56 (4), 041308.

Mery, D., Svec, E., Arias, M., Riffo, V., Saavedra, J.M., Banerjee, S., 2016. Modern computer vision techniques for X-ray testing in baggage inspection. IEEE Trans. Syst. Man Cybern.: Syst. 47 (4), 682–692.

Mood, A.M., Graybill, F.A., Boes, D.C., 1974. Introduction to the Theory of Statistics, third ed. McGraw-Hill, Tokyo.

Moon, S., Choi, S., Jang, H., Shin, M., Roh, Y., Baek, J., 2021. Geometry calibration and image reconstruction for carbon-nanotube-based multisource and multidetector CT. Phys. Med. Biol. 66 (16), 165005.

Moshkbar-Bakhshayesh, K., Afarideh, H., Azimirad, R., 2023. Inspection of cargo using dual-energy X-ray radiography: A review. Radiat. Phys. Chem. 111180.

Neculaes, V.B., Edic, P.M., Frontera, M., Caiafa, A., Wang, G., De Man, B., 2014. Multisource X-ray and CT: Lessons learned and future outlook. IEEE Access 2, 1568–1585.

Osipov, S., Usachev, E.J., Chakhlov, S., Schetinkin, S., Osipov, O., 2020. Inspection of bulk cargoes and liquids by the dual energy method. Radiat. Phys. Chem. 177, 109133.

Petrozziello, A., Jordanov, I., 2019. Automated deep learning for threat detection in luggage from X-ray images. In: International Symposium on Experimental Algorithms. Springer, pp. 505–512.

Quan, E., Lalush, D.S., 2007. Evaluation of hexagonal and square geometries for motion-free arrayed-source X-ray micro-CT. In: 2007 4th IEEE International Symposium on Biomedical Imaging: From Nano to Macro. IEEE, pp. 221–224.

Quan, E.M., Lalush, D.S., 2010. Three-dimensional imaging properties of rotation-free square and hexagonal micro-CT systems. IEEE Trans. Med. Imaging 29 (3), 916–923.

Riffo, V., Mery, D., 2012. Active X-ray testing of complex objects. Insight - Non-Destr. Test. Cond. Monit. 54 (1), 28–35.

Rogers, T.W., Jaccard, N., Morton, E.J., Griffin, L.D., 2017. Automated X-ray image analysis for cargo security: Critical review and future promise. J. X-Ray Sci. Technol. 25 (1), 33–56.

Salamon, M., Reims, N., Böhnel, M., Zerbe, K., Schmitt, M., Uhlmann, N., Hanke, R., 2016. XXL-CT capabilities for the inspection of modern electric vehicles. In: 19th World Conference on Non-Destructive Testing.

Salamon, M., Reims, N., Prjamkov, D., Schmitt, M., Makarov, J., Ak, D., Kronenberger, M., Schladitz, K., Redenbach, C., Grzesiak, S., et al., 2025. Gulliver–A new kind of industrial CT. e-J. Nondestruct. Test. 30 (2).

Shao, F., Liu, J., Wu, P., Yang, Z., Wu, Z., 2022. Exploiting foreground and background separation for prohibited item detection in overlapping X-Ray images. Pattern Recognit. 122, 108261.

Shikhaliev, P.M., 2018. Large-scale MV CT for cargo imaging: A feasibility study. Nucl. Instrum. Methods Phys. Res. Sect. A: Accel. Spectrom. Detect. Assoc. Equip. 904, 35–43.

Sprenger, F., Calderon-Colon, X., Cheng, Y., Englestad, K., Lu, J., Maltz, J., Paidi, A., Qian, X., Spronk, D., Sultana, S., et al., 2010. Distributed source X-ray tube technology for tomosynthesis imaging. In: Medical Imaging 2010: Physics of Medical Imaging. Vol. 7622, SPIE, pp. 1751–1758.

Spronk, D., Luo, Y., Inscoe, C.R., Lee, Y.Z., Lu, J., Zhou, O., 2021. Evaluation of carbon nanotube x-ray source array for stationary head computed tomography. Med. Phys. 48 (3), 1089–1099.

Sugie, H., Tanemura, M., Filip, V., Iwata, K., Takahashi, K., Okuyama, F., 2001. Carbon nanotubes as electron source in an X-ray tube. Appl. Phys. Lett. 78 (17), 2578–2580.

Valković, V., Blagus, S., Sudac, D., Nađ, K., Matika, D., 2004. Inspection of shipping containers for threat materials. Radiat. Phys. Chem. 71 (3–4), 897–898.

Van Aarle, W., Palenstijn, W.J., Cant, J., Janssens, E., Bleichrodt, F., Dabravolski, A., De Beenhouwer, J., Batenburg, K.J., Sijbers, J., 2016. Fast and flexible X-ray tomography using the ASTRA toolbox. Opt. Express 24 (22), 25129–25147.

van den Bos, A., 2007. Parameter Estimation for Scientists and Engineers. John Wiley & Sons.

Wu, W., Zhang, J., Wang, S., Chen, J., 2023. Flat-panel addressable cold-cathode X-Ray source-based stationary CT architecture. IEEE Trans. Instrum. Meas. 72, 1–9.